

A SPITZER SPACE TELESCOPE SURVEY FOR DUSTY DEBRIS DISKS IN THE NEARBY 32 ORIONIS GROUP

ALEXANDER J. SHVONSKI^{1,2}, ERIC E. MAMAJEK^{1,3}, JINYOUNG SERENA KIM⁴, MICHAEL R. MEYER⁵, AND MARK J. PECAUT⁶

¹Department of Physics & Astronomy, University of Rochester, Rochester, NY, 14627-0171, USA

²Current address: Department of Physics, Boston College, 140 Commonwealth Ave., Chestnut Hill, MA, 02467, USA

³Current address: Jet Propulsion Laboratory, California Institute of Technology, M/S 321-100, 4800 Oak Grove Dr., Pasadena, CA 91109, USA

⁴Steward Observatory, University of Arizona, Tucson, AZ, 85721, USA

⁵University of Michigan, Department of Astronomy, 1085 S. University, Ann Arbor, MI 48109, USA and

⁶College of Arts and Sciences, Rockhurst University, 1100 Rockhurst Rd., Kansas City, MO 64110, USA

Unpublished

ABSTRACT

We report *Spitzer Space Telescope* IRAC 3.6, 4.5, 5.8 and 8 μm and MIPS 24 and 70 μm observations of the 32 Ori Group, a recently discovered nearby stellar association situated towards northern Orion. The proximity of the group (~ 93 pc) has enabled a sensitive search for circumstellar dust around group members, and its age (~ 20 Myr) corresponds roughly to an epoch thought to be important for terrestrial planet formation in our own solar system. We quantify infrared excess emission due to circumstellar dust among group members, utilizing available optical (e.g. Hipparcos, Tycho) and near-IR (2MASS) photometry in addition to the *Spitzer* IR photometry. We report 4 out of the 14 objects which exhibit 24 μm excess emission more than 4σ above the stellar photosphere ($>20\%$) though lacking excess emission at shorter wavelengths: HD 35656 (A0Vn), HD 36338 (F4.5), RX J0520.5+0616 (K3), and HD 35499 (F4). Two objects (HD 35656 and RX J0520.0+0612) have 70 μm excesses, although the latter lacks 24 μm excess emission. The 24 μm disk fraction of this group is $29^{+14}_{-9}\%$, which is similar to previous findings for groups of comparable ages and places 32 Ori as the young stellar group with the 2nd most abundant 24 μm excesses among groups lacking accreting T Tauri stars (behind only the approximately β Pic moving group). We also model the infrared excess emission using circumstellar dust disk models, placing constraints on disk parameters including L_{IR}/L_* , T_{disk} , characteristic grain distance, and emitting area. The L_{IR}/L_* for all the stars can be reasonably explained by steady state disk evolution.

Keywords: Infrared: (stars, planetary systems) – open clusters and associations: individual: (32 Ori group) – Stars: (circumstellar matter, pre-main sequence)

1. NOTE TO READERS

This report represents the final report for the master's degree research of Alex Shvonski in the Department of Physics & Astronomy, University of Rochester. Preliminary results from this survey were presented in a AAS poster (Shvonski et al. 2010). The first author has moved on from astronomical research, and the other coauthors have not had the time to bring the analysis and text up to date. Given the new astrophysical interest in the new, nearby young stellar group associated with 32 Ori, and interest in the stellar and disk properties of its membership, the authors have agreed to post this unrefereed paper to arXiv in its original form from 2010 (excepting comments in italics). Note that a forthcoming paper by Bell, Murphy, and Mamajek (submitted to MNRAS) will present and improved age estimate for the 32 Ori group, a survey for new low-mass members, and analysis of the WISE infrared photometry. Revised estimates for the interstellar reddening for the 32 Ori group members are much smaller ($E(B-V) \simeq 0.03$ mag) than that calculated for the cool stars in this 2010 study. The original study used intrinsic colors appropriate for dwarfs, however using an intrinsic color sequence appropriate for pre-MS stars (Pecaut & Mamajek 2013) now results in consistently lower reddening values calculated for both the hot and cool stellar populations. Also, the age scale for the <40 Myr-old groups plotted in Figure 7 is already obsolete, with the ages of some of the groups having been recently revised upward by ~ 50 -100% (e.g. Pecaut et al. 2012; Bell et al. 2015;

Pecaut & Mamajek 2016).

2. INTRODUCTION

It is widely established that circumstellar disks are progenitors of planetary systems, although the evolution of such systems is less understood. A large fraction of stars, thought to be close to unity, initially contain circumstellar material and then lose their disks over time, possibly through processes like accretion, planet formation, photoevaporation, etc. (Meyer et al. 2007). Primordial disks become gas-depleted on a timescale of ~ 1 -10 Myr (Haisch et al. 2001; Hillenbrand 2005), and plots of primordial disk fraction versus age show an approximately exponential decay with a characteristic timescale of $\tau \simeq 2.5$ Myr (Mamajek 2009). The prevalence of gas-depleted (debris) disks suggests that the collisional grinding of planetesimals is responsible for dust production, since grain removal processes such as radiation pressure and Poynting-Robertson drag would not otherwise allow dust to persist for timescales observed (Backman & Paresce 1993). Mid-infrared (mid-IR) excess emission from micron-sized grains in these debris disks is a successful disk diagnostic that can be used to characterize individual objects and examine trends including debris disk frequency vs. age (e.g. Hillenbrand 2008). Of primary importance are studies of young stellar groups (i.e. clusters and/or associations) of disparate ages, which provide snapshots of the disk dispersal process from which we can infer evolutionary trends.

Placing our own solar system in context, the timescale between ~ 10 -50 Myr is a particularly interesting and dynamic epoch of planetary evolution (Canup 2004). Radionuclide data (Hf-W chronometry) suggests that the proto-Earth was impacted by a Mars-sized body which formed the moon at an age of ~ 25 -30 Myr (Canup 2004). The frequency and characteristics of debris disks at such ages has potential implications for models of our own solar system. However, well-characterized samples of stellar associations with ages of < 10 -50 Myr are rare within a few hundred pc of the Sun. This study contributes a snapshot of circumstellar disk evolution among a new nearby sample of young stars in this age range.

We report on a *Spitzer* IRAC and MIPS survey of debris disks for 14 members of the recently identified nearby young 32 Ori group. In §3 we discuss the current evidence for a young group associated with 32 Ori, first identified by Mamajek (2007a). In §4 we summarize our observations, including optical spectroscopy, IRAC, and MIPS data, and additional optical and IR data (i.e. Hipparcos, Tycho, 2MASS, IRS spectra). In §5 we identify disk candidates by examining color-color relations. In §6 we model stellar photospheric emission, compute stellar luminosities, and place group members on an HR diagram to determine the age of the group. We then characterize mid-IR excess emission using dust disk models. Finally, in §7 we discuss the disk fraction within the 32 Ori association and place our results in the broader context of circumstellar disk evolution, and summarize our findings in §8.

3. THE 32 ORI GROUP

Mamajek (2007a) presented evidence for a young stellar group associated with the B-type star 32 Ori that would appear to constitute the first northern, young (< 100 Myr) stellar group discovered within 100 pc of the Sun. It is a previously unrecognized stellar group situated towards northern Orion, but at only $\sim 1/5$ th the distance of the well-studied λ Ori and Ori OB1 star-forming regions (~ 400 pc; < 10 -15 Myr-old, Hernández et al. 2006). With a distance of ~ 93 pc and age of ~ 20 Myr (Mamajek 2007a), the 32 Ori Group appears to be unrelated to any star-forming regions. As the reality of the group, and our assessment of its membership and age, is critical to our study, we present a more thorough characterization.

The group was originally identified by Mamajek (2007a) as a strong concentration of comoving stars in a vector-point diagram (proper motion in R.A. vs. proper motion in Dec.) of young stars in northern Orion (see Fig. 1). While the more distant λ Ori and Ori OB1a members in northern Orion have very small proper motions (< 5 mas yr $^{-1}$), surrounding the nearby B5+B7 binary 32 Ori ($\varpi = 10.77 \pm 0.64$ mas; $d = 93^{+6}_{-5}$ pc; van Leeuwen 2007) is a clump of bright A-stars and X-ray-emitting late type stars (candidate young stars) with proper motions consistent with $(\mu_\alpha, \mu_\delta) \simeq (+8, -35)$ mas yr $^{-1}$. The trigonometric parallaxes of the bright B/A-type stars in the original (Perryman & ESA 1997) and revised (van Leeuwen 2007) are consistent with being approximately co-distant at ~ 93 pc (within their parallax uncertainties), although main sequence fitting suggests more like 100 pc. Some of the comoving X-ray-luminous stars were previously discovered to be Li-rich in spectroscopic follow-up of ROSAT All-Sky Survey (RASS) X-ray sources

Table 1
2MASS Identifiers for 32 Ori Group Candidate Members

ID	2MASS
32 Ori	J05304706+0556536
2UCAC 33699961	J05194398+0535021
2UCAC 33878694	J05253253+0625336
HBC 443	J05343491+1007062
HD 35499	J05251457+0411482
HD 35656	J05263883+0652071
HD 35695	J05265202+0628227
HD 35714	J05265999+0710131
HD 36338	J05311570+0539461
RX J0520.0+0612	J05200029+0613036
RX J0520.5+0616	J05203182+0616115
RX J0523.7+0652	J05234246+0651581
RX J0529.3+1210	J05291899+1209295
HD 245567	J05371844+1334525

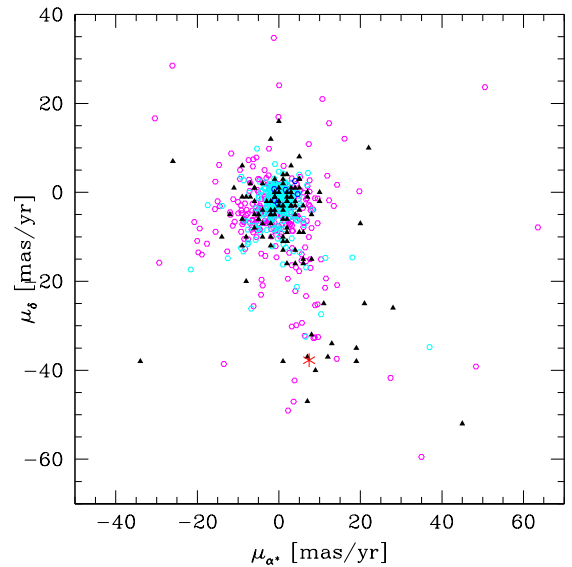


Figure 1. Reproduction of the proper motion plot from Mamajek (2007a) indicating the presence of a young nearby stellar group associated with 32 Ori. 32 Ori is marked as a red asterisk. Pre-MS stars within 10° of 32 Ori in the Ducourant et al. (2005) catalog are plotted as filled triangles. Hipparcos stars (Perryman & ESA 1997) within 10° of 32 Ori of O-type (dark blue open circles), B-type (light blue open circles), and A-type (magenta open circles). Note the swarm of pre-MS stars with proper motions similar to that of 32 Ori. The clump of hot stars and pre-MS stars with negligible proper motions are associated with Ori OB1 ($d \simeq 400$ pc).

by Alcalá et al. (1996, 2000). A subset of the Alcalá et al. RASS sources are very Li-rich, and share the same radial velocity as 32 Ori (~ 18 km s $^{-1}$). Accurate proper motions from new astrometric catalogs (e.g. UCAC; Zacharias et al. 2004; Zacharias et al. 2010) show that some of these RASS stars in Orion are co-moving, and are much closer than the Orion star-forming region. Recent observations by using the FAST spectrograph on the Mt. Hopkins 1.5m (60") telescope have led to the identification of a few new, pre-MS members (§4.1).

4. OBSERVATIONS & DATA REDUCTION

4.1. Optical Spectroscopy

Optical spectra of the stars listed in Table 1 were obtained with the FAST instrument on the Tillinghast 1.5-m telescope at the Fred Lawrence Whipple Observatory in queue mode on UT 25 and 27 Jan 2006. The spectra cover $\sim 3500\text{--}7400\text{\AA}$ with a resolution of $\sim 3\text{\AA}$ and were visually examined using the *sptool* spectral comparison program described in Pecaut et al. (2012) to obtain spectral types. A dense grid of MK spectral standards (and references therein; Gray & Corbally 2009)¹ was assembled using spectra taken at similar resolution from the CTIO 1.5-m telescope and Nstars website².

Several cool stars exhibit $H\alpha$ emission indicative of enhanced chromospheric activity. One M-type member 2UCAC 33699961, has $H\alpha$ emission that is relatively high ($EW \sim 10.5\text{\AA}$) but is still consistent with chromospheric activity rather than accretion (Barrado y Navascués & Martí 2003). We also measured Li equivalent widths for each object from the Li I $\lambda 6707\text{\AA}$ feature as a youth indicator. Red optical spectra and equivalent widths for $H\alpha$ and Li I $\lambda 6707\text{\AA}$ for the K/M-type 32 Ori members are presented in Figure 1. Equivalent widths were measured in IRAF³. The two M3-type stars show very strong chromospheric activity ($H\alpha$ emission) but depleted Li. This suggests that the stars are young, but probably older than 10^7 yr (older than η Cha and TW Hya groups; Mentuch et al. 2008).

4.2. IRAC

4.2.1. Observations

Spitzer IRAC observations were obtained 16–17 October 2007 at 3.6, 4.5, 5.8 and $8\text{ }\mu\text{m}$ in stellar mode for 11 objects. Additional data for HBC 443 and HD 245567 was retrieved from the *Spitzer* archive (program ID 37, PI Giovanni Fazio; program ID 148, PI Michael R. Meyer, respectively). Observations of HBC 443 were taken in high dynamic range (HDR) mode on 12 October 2004, while observations of HD 245567 were taken in subarray mode 8 October 2004. Observations of HD 245567 were not taken at $5.8\text{ }\mu\text{m}$. IRAC observations for 32 Ori were not taken, however, we obtained IRS data from the literature, which will be discussed in §4.5. IRAC subarrays are 32×32 pixel sections of the full array, which is 256×256 pixels in size with a pixel scale of $\sim 1.2''$ pix^{-1} (IRAC Data Handbook 3.0⁴).

The primary reason for the IRAC observations is to complement the 2MASS photometry to predict stellar photospheric emission at 24 and $70\text{ }\mu\text{m}$. There is a chance of an excess due to warm dust in the IRAC bands, however this is very unlikely given that the group is >10 Myr old (e.g. Mamajek et al. 2004). We aimed to detect the stellar photosphere at a minimum S/N of 50, thereby ensuring similar relative accuracy as the 2MASS JHK fluxes. Exposure times in stellar mode were 0.4 sec for IRAC channels 1 and 2 and

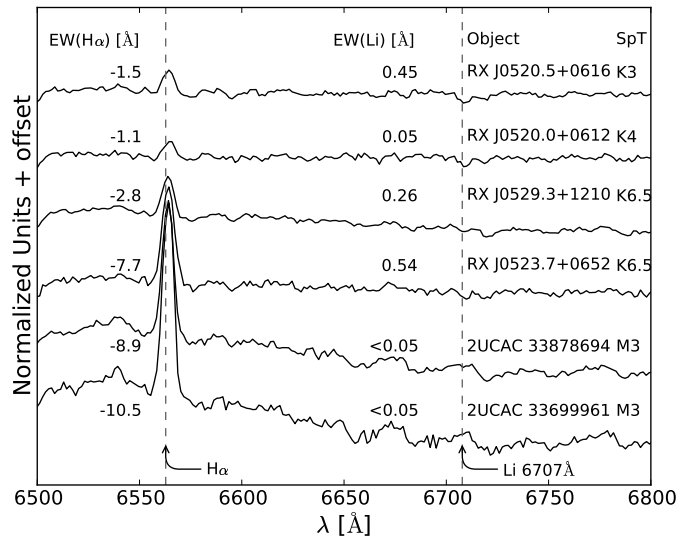


Figure 2. Optical spectra of late-type ($>K0$) group members. $H\alpha$ emission indicative of enhanced chromospheric activity is clearly apparent.

2 sec for channels 3 and 4. Using a 9 position random dither pattern, this resulted in integration times of 3.6 sec and 18 sec for the respective channels.

4.2.2. Image Processing

For all 13 objects, IRAC images were processed with the *Spitzer* Science Center (SSC) pipeline version S18.7.0. This pipeline produces basic calibrated data (BCD) images, for which reduction steps including dark subtraction and a flat-field correction are carried out (IRAC Data Handbook 3.0). The “mux-bleed” effect is also corrected in stellar and HDR mode, but not in subarray mode. Additionally, nonlinear pixel responses and cosmic ray detections are flagged in an image mask (IRAC Data Handbook 3.0).

BCD images were processed using the SSC package MOPEX (Makovoz & Marleau 2005). Briefly, we discuss the data reduction steps implemented using this package.⁵ For each object, background matching between overlapping input frames was performed by computing additive offsets for each image. First, the median value in a 45×45 pixel window was subtracted at each pixel location in every image in order to assist in the detection of bright sources, which were not included in background matching estimates. Bright sources were detected in background subtracted images through image segmentation, and these sources were masked during background matching. Background subtracted images were projected onto a Fiducial Image Frame (FIF), which defines the overlap between all images. Ultimately, offsets were computed by minimizing the differences between overlapping pixels and requiring that the sum of the offsets equal zero. Offsets that were 3σ outliers were not included in computing the offsets for other images.

Before photometry was performed on background matched images, they were used to create a set of outlier masks. Multi-frame outlier detection was performed by filtering individual

¹ Extensive notes on the pedigrees of all known dwarf, subgiant, and giant MK standard stars can be found at: <http://www.pas.rochester.edu/emamajek/spt/>

² <http://stellar.phys.appstate.edu>

³ IRAF is distributed by the National Optical Astronomy Observatory, which is operated by the Association of Universities for Research in Astronomy, Inc., under cooperative agreement with the National Science Foundation.

⁴ See <http://ssc.spitzer.caltech.edu/irac/iracinstrumenthand-book/>

⁵ The following steps were adopted from the MOPEX User’s Guide 18.3.2, which can be found at <http://ssc.spitzer.caltech.edu/dataanalysis/tools/mopex/mopexusers-guide/>

pixels at common spatial locations in background corrected images for time dependent phenomena. The median absolute deviation of individual pixels was computed and outliers deviating more than 5 times this value from the median were rejected. The results of multiframe outlier detection were used to create an “rmask.” Pixels masked in the rmask were reinterpolated in the background matched images. In addition to rmask, pmasks (containing permanently damaged pixels), and DCE (data collection event) status masks (containing temporarily damaged pixels) are also used to mask pixels.

Additional care must be taken for the reduction of IRAC images. The position of the IRAC instrument causes a variation in pixel solid angle of order $\sim 1.5\%$ across each channel (IRAC Data Handbook 3.0). Additionally, the effective filter bandpass varies across the array of each IRAC channel, producing differences in flux of order $\sim 10\%$ (IRAC Data Handbook 3.0; Quijada et al. 2004). Thus, there are two important corrections that must be performed on BCD data: a pixel solid angle correction (PSAC)⁶ and an array-location-dependent optical distortion correction (ALDODC)⁷.

Corrections that account for optical distortion and pixel solid angle variations across IRAC arrays are encoded in the headers of BCD images (IRAC Data Handbook 3.0). The SSC provides ALDODC images, which also include PSAC information in their headers. Therefore, we divided the ALDODC images by the PSAC images before applying this correction, so that the PSAC was not applied twice. An important caveat to the above corrections is that they are only applicable to objects emitting in the Rayleigh-Jeans regime at IRAC wavelengths (e.g. photospheric emission from point-sources) (IRAC Data Handbook 3.0). Since 32 Ori members, due to their age, most likely do not have warm inner disks, we expect that their emission will be purely photospheric and no additional precautions will need to be heeded.

4.2.3. Photometry

Photometry was performed using the APEX routine `aperture.pl`, using an aperture radius of 3 image pixels and a sky annulus of 12-20 image pixels. This routine computes aperture photometry for a specified point in a set of images; it applies pmasks, DCE status masks, and rmask, as described in the previous section. As input, we used the background matched BCD images corrected for pixel solid angles and optical distortion. We used the median fluxes obtained from sets of corrected images as final values and standard errors as measures of uncertainty. Additionally, there exist uncertainties in the calibration factor used to convert instrumental units to MJy/sr. Uncertainties for channels 1-4 are 1.8%, 1.9%, 2.0%, and 2.1%, respectively (Reach et al. 2005). Carpenter et al. (2008) compared the flux density calibrations used by Reach et al. (2005) in full-array mode with sub-array data to determine if there exist relative offsets in any IRAC channels. They determined that differences are of order $<1\%$ and, therefore, inconsequential. Thus, we perform no additional correction to data taken in sub-array mode.

⁶ Correction images are available at <http://ssc.spitzer.caltech.edu/irac/calibrationfiles/solidangles/>

⁷ Correction images are available at <http://ssc.spitzer.caltech.edu/irac/calibrationfiles/locationcolor/>

Aperture corrections for all IRAC channels were obtained from the IRAC Data Handbook 3.0; they are 1.112, 1.113, 1.125, and 1.218 for channels 1, 2, 3, and 4, respectively. We used zero-point fluxes reported in the IRAC Data Handbook 3.0 to convert flux measurements to magnitudes.

4.3. MIPS 24 μm

4.3.1. Observations

Spitzer MIPS observations were obtained 16-17 March 2008 at 24 and 70 μm in photometry mode. A total of 12 objects were imaged at 24 μm and 13 objects (including 32 Ori) were imaged at 70 μm . Additional 24 and 70 μm data for one object, HD 245567 (observed 13 October 2004), were obtained from the *Spitzer* archive (program ID 148, PI Michael R. Meyer). In this section, we describe data reduction and photometry performed on the 24 μm data; the 70 μm data are discussed in section 4.

The MIPS 24 μm array is 128x128 pixels in size with a field of view of $\sim 5.4' \times 5.4'$, giving it a scale of $2.49'' \times 2.60'' \text{ pix}^{-1}$ (MIPS Data Handbook 3.3.1⁸). Our goal was to detect stellar photospheres at minimum S/N of 10, where the predicted photospheric fluxes range from ~ 1.00 to 18.65 mJy for our targets. Thus, we performed 3 sec integrations for B through early-K type stars, using either 2 or 4 cycles, and 10 sec integrations for later type stars, using up to 18 cycles for an M3 star.

4.3.2. Image Processing

For 12 objects, MIPS 24 μm images were processed with the SSC pipeline version S17.0.4. SSC pipeline version S16.1.0 was used to process HD 245567 data. Similarly, these pipelines produce basic calibrated data (BCD) images, which were processed using the SSC package MOPEX (Makovoz & Marleau 2005) in the same manner as the IRAC data. An additional step was taken to create mosaic images from background matched BCD images, which were used for point source detection in APEX. Mosaic images for each object were created by first applying rmask, pmask, and DCE status masks and then combining images using average pixel values. MIPS data does not require additional corrections from optical distortion and variations in pixel solid angle; therefore, we did not apply PSAC or ALDODC images.

4.3.3. Photometry

Multiframe point source extraction was implemented using the SSC APEX package. In this process, sources are detected using the mosaic image while a PRF is simultaneously fit to a stack of inputs images, ultimately giving a flux density for detected sources. We utilized the following procedure.⁹ First, background subtraction of the mosaicked images was performed using a median value computed from a 25×25 pixel window at each pixel in preparation for point source

⁸ <http://ssc.spitzer.caltech.edu/mips/mipsinstrumenthandbook/>

⁹ see MOPEX User's Guide 18.3.2 for a complete discussion of PRF fitting.

Table 2
Spitzer IRAC & MIPS Photometry

ID	2MASS	[3.6] (mag)	[4.5] (mag)	[5.8] (mag)	[8.0] (mag)	[24] (mJy)	[70] (mJy)
32 Ori	J05304706+0556536	9.8±2.3
2UCAC 3369961	J05194398+0535021	9.76±0.04	9.72±0.07	9.70±0.02	9.68±0.04	1.10±0.01	-2.8±1.6
2UCAC 33878694	J05253253+0625336	9.56±0.03	9.58±0.04	9.50±0.03	9.50±0.02	1.17±0.02	-6.8±3.0
HBC 443	J05343491+1007062	7.36±0.02	7.35±0.02	7.39±0.09	7.33±0.04	8.94±0.14	6.4±6.0
HD 35499	J05251457+0411482	7.48±0.01	7.49±0.01	7.52±0.01	7.48±0.03	8.45±0.10	1.8±1.3
HD 35656	J05263883+0652071	6.48±0.01	6.48±0.02	6.51±0.01	6.47±0.00	88.45±0.36	91.0±4.2
HD 35695	J05265202+0628227	7.67±0.03	7.67±0.02	7.67±0.01	7.64±0.01	6.30±0.20	13.1±5.9
HD 35714	J05265999+0710131	6.75±0.02	6.76±0.02	6.77±0.01	6.78±0.01	13.33±0.13	1.1±2.3
HD 36338	J05311570+0539461	7.41±0.02	7.41±0.01	7.42±0.00	7.41±0.01	14.79±0.15	8.6±2.9
RX J0520.0+0612	J05200029+0613036	8.53±0.02	8.55±0.02	8.52±0.02	8.48±0.01	2.91±0.06	7.9±1.7
RX J0520.5+0616	J05203182+0616115	8.49±0.02	8.49±0.03	8.45±0.02	8.41±0.01	3.87±0.09	-3.5±1.9
RX J0523.7+0652	J05234246+0651581	8.94±0.02	8.93±0.03	8.90±0.02	8.87±0.02	1.99±0.03	7.8±3.1
RX J0529.3+1210	J05291899+1209295	9.02±0.02	9.03±0.04	9.00±0.03	8.99±0.01	1.63±0.03	11.0±8.3
HD 245567	J05371844+1334525	7.51±0.02	7.52±0.03	...	7.50±0.09	6.87±0.09	-24.9±5.7

Note. — “...” represent photometry that we did not obtain. Additional absolute calibration uncertainties of 1.8%, 1.9%, 2.0%, 2.1%, 4%, and 7% for respective IRAC and MIPS channels (MIPS Data Handbook 3.3.1; Reach et al. 2005; Engelbracht et al. 2007) should be added in quadrature with the photometric uncertainties reported here.

detection. Next, non-linear matched filtering was performed on the background subtracted images in order to improve the detectability of point sources. Point source probability (PSP) images, which measure the probability that there is a point source above the noise level at each pixel, were created. These images were used as input into the detect module, which performs image segmentation to detect sources above a 4σ threshold. Similar to the process of point source *detection*, the stack of input images was background subtracted in preparation for point source *estimation* using a median value computed from a 45×45 pixel window at each pixel. PRF fitting was performed on these images using a 7×7 pixel fitting area.

Carpenter et al. (2008) noted that the uncertainties computed by the APEX module are intrinsically smaller than errors computed from the repeatability of observations. Thus, we computed standard errors from aperture photometry performed on individual BCD images and adopted these values as a measure of repeatability; aperture photometry was performed using the APEX routine `aperture.pl`. As done with IRAC images, background matched BCD images were masked using `pmasks`, `status masks`, and `rmasks`. For all sources except HD 35656, a smaller aperture radius of $3.5''$ and annulus size of $20''$ - $32''$ were used, with a corresponding aperture correction of 2.57. For HD 35656, a larger aperture radius of $7''$ and annulus of $20''$ - $32''$ were used, with a corresponding aperture correction of 1.61. Aperture corrections were obtained from the MIPS Data Handbook 3.3.1. Additionally, we adopted a $24\mu\text{m}$ calibration uncertainty of 4% (Engelbracht et al. 2007).

We found that PRF estimates of flux density deviated from aperture photometry measurements by $<10\%$ for all objects except for RX J0529.3+1210. This star was identified as a spectroscopic binary by Mace et al. (2009), and was located in a region of complex nebulousity, which compounded the difficulty in obtaining accurate photometry.

4.4. MIPS $70\mu\text{m}$

4.4.1. Observations

We obtained $70\mu\text{m}$ data in wide photometry mode, where the array of 32×32 pixels has a scale of $9.85''\times 10.06''\text{ pix}^{-1}$. Again, 13 objects were observed while data for HD 245567

was obtained from the *Spitzer* archive.

We realized that reaching the photosphere for all of our objects, ranging in spectral type from B-M, at $70\mu\text{m}$ was unfeasible, so we instead adopted a uniform survey depth of 18 cycles of 10 sec frame time for each star, giving approximate 1σ point source sensitivities of $\sim 3\text{ mJy}$ for our background levels. In the absence of a disk, the brightest star (32 Ori; $F_{70,\text{phot}} \sim 10\text{ mJy}$) would have its photosphere detected at $\sim 4\sigma$ with this observing sequence; however, the photospheres of the other objects ($F_{70,\text{phot}} \sim 0.1$ - 2.1 mJy) are below this 1σ limit. A disk emitting at $\sim 9000\text{ Z}$ ($Z = 1\text{ zody} = 1.125\times 10^{21}\text{ cm}^2$; Gaidos 1999) would be detectable at 3σ around our targets, assuming a $70\mu\text{m}$ Wien temperature. For comparison, a survey of similar depth in the similarly aged cluster NGC 2547 ($d=450\text{ pc}$; Young et al. 2004) could detect only disks emitting at $> 2\times 10^5\text{ Z}$.

4.4.2. Image Processing

All MIPS $70\mu\text{m}$ images were processed with the SSC pipeline version S17.0.4 except HD 245567, for which pipeline version S16.1.0 was used. This work utilized filtered basic calibrated data (FBCD), produced by subtracting the temporal median of adjacent DCEs from each pixel in order to account for latent phenomena (MIPS Data Handbook 3.3.1). FBCD images were processed using the SSC package MOPEX (Makovoz & Marleau 2005) in the same manner as the $24\mu\text{m}$ data in order to create mosaic images.

4.4.3. Photometry

Aperture photometry was performed on the mosaicked images in IRAF using an aperture radius of $16''$ and an annulus size of $18''$ - $39''$, corresponding to $2\times\text{FWHM}$ (MIPS Data Handbook 3.3.1). This method is preferable to PRF fitting because most sources are not detectable in individual FBCD images. Apertures were centered on positions determined from the detection procedure in the $24\mu\text{m}$ APEX module. An aperture correction of 2.07 was adopted from the MIPS Data Handbook 3.3.1, corresponding to a 60 K blackbody.

RX J0520.5+0616 appears to have been contaminated by a nearby (likely) extragalactic source. We performed PRF

fitting and subtraction of the source and redid the $70\mu\text{m}$ photometry, as described above. This step was not needed at $24\mu\text{m}$ because of the simultaneous PRF fitting that was performed. The nearby object was not visible at near-IR wavelengths. No spurious point sources were detected with the aperture/annulus around other objects.

The uncertainties in the $70\mu\text{m}$ images were computed following the prescription of Carpenter et al. (2008). We used the following equation:

$$\sigma = (\eta_{\text{sky}}\eta_{\text{corr}})(\Omega\Sigma_{\text{sky}})\sqrt{N_{\text{ap}} + N_{\text{ap}}^2/N_{\text{sky}}} \quad (1)$$

The values in equation (1) are the number of pixels in the aperture N_{ap} , the number of pixels in the annulus N_{sky} , the solid angle/pixel Ω , the noise/pixel within the sky annulus Σ_{sky} , the correlation correction for adjacent pixels η_{corr} , and the correction for systematic differences between aperture and annulus background noise η_{sky} . The first four values were computed in IRAF. The correlation correction is necessary because FBCD images are interpolated in order to produce a final mosaic that is 2.5 times larger than the initial images (i.e. FBCDs of $9.8''$ pixel $^{-1}$ are transformed to a scale of $4''$ pixel $^{-1}$). Thus, the correlation correction is $\eta_{\text{corr}}=2.5$. The correction for disparate aperture/annulus noise is necessary because there exists higher noise in pixel columns near the source position; Carpenter et al. (2008) concluded that this effect was due to latent phenomena from calibration stim flashes. We adopt their value of $\eta_{\text{sky}}=1.40$. The additional flux calibration uncertainty of 7% was used (MIPS Data Handbook 3.3.1).

4.5. Additional Photometry

We obtained B and V -band photometry and photometric errors from the Hipparcos (Perryman & ESA 1997) and Tycho-2 catalogues (Høg et al. 2000). We converted Tycho-2 photometry to the Johnson/Cousins system using the polynomial fits from Mamajek et al. (2002, 2006). For 32 Ori, we retrieved two additional IR fluxes from Chen et al. (2006), which correspond to the photometric bands $8.5\text{--}13\mu\text{m}$ and $30\text{--}34\mu\text{m}$, computed from IRS spectra. The fluxes, which are not listed in Table 1, are 468 ± 0.5 mJy and 50.4 ± 1.7 mJy, respectively, and have calibration errors of 5% (Chen et al. 2006).

5. IDENTIFYING DISK CANDIDATES

5.1. IRAC Excesses

Longer wavelength emission probes increasingly cooler circumstellar material at larger radii. Excess emission at IRAC wavelengths likely originates from a region close to the star ($<1\text{AU}$) (e.g. Balog et al. 2009) and is, therefore, a warm inner disk diagnostic. Color-color diagrams indicate whether objects exhibit redder colors than an intrinsic photospheric value given their spectral type, where $V-K_s$ serves as a stellar temperature indicator. 3.6 , 5.8 , and $8\mu\text{m}$ photospheric excesses for group members were determined from $V-K_s$ versus $K_s-[\lambda_{\mu\text{m}}]$ color-color diagrams (Fig. 2). We adopted intrinsic stellar color loci of Balog et al. (2009) for all of these plots. The loci were derived by fitting a second degree polynomial to color-color diagrams of ~ 140 members of

NGC 2457A and B (Balog et al. 2009).

Clearly, these figures indicate that no objects exhibit excess emission above the photosphere at IRAC wavelengths, as no objects appear statistically significantly redder than their intrinsic stellar loci. We anticipate no near-IR excesses due to the age of the 32 Ori group (e.g. Mamajek et al. 2004). Ultimately, this analysis is consistent with spectroscopic results and implies that group members are not accreting T Tauri stars and do not have detectable warm inner dust disks.

5.2. MIPS Excesses

Figure 2 shows the $V-K_s$ versus $K_s-[24]$ color-color diagram for 32 Ori members. We adopted the intrinsic color locus of Balog et al. (2009), derived from 1500 stars from numerous *Spitzer* debris disk programs. Balog et al. (2009) fit a seventh-order polynomial (eq. 2) to the color-color locus and determined an rms scatter of $\sim 3\%$.

$$\begin{aligned} (K_s-[24])_0 = & -0.024 + 0.0025(V-K)_0 \\ & + 0.001(V-K_s)_0^2 + 0.0005(V-K_s)_0^3 \\ & + 0.00012(V-K_s)_0^6 - 0.000019(V-K_s)_0^7 \end{aligned} \quad (2)$$

It is apparent from Figure 2 that several 32 Ori members exhibit $24\mu\text{m}$ photospheric excesses. We determined that 4 members, namely HD 35656 (A0Vn), HD 36338 (F4.5), RX J0520.5+0616 (K3), and HD 35499 (F4), have excess emission more than 4σ ($\geq 20\%$) above their stellar photospheres, indicating that these members are debris disk candidates. Additionally, 3 of these 4 members (excluding HD 35499) have excess emission more than $\geq 38\%$ above their photospheres. Thus, the disk fraction within this group at the 4σ excess level is 29% (+14%, -9%; 1σ upper/lower limits, respectively), using binomial statistics (Burgasser et al. 2003).

We determined $70\mu\text{m}$ photospheric excesses by assuming a Rayleigh-Jeans dependence, which implies that $F_{70,\text{phot}} = F_{24,\text{phot}}(24/70)^2$. Thus, the only parameter required to determine $F_{70,\text{phot}}$ was the $24\mu\text{m}$ photospheric flux derived from the Balog et al. (2009) color-color locus. We found that 2 objects had $70\mu\text{m}$ excess emission $>4\sigma$ above their photospheric values: HD 35656, which also exhibited a $24\mu\text{m}$ excess, and RX J0520.0+0612, which did not exhibit a $24\mu\text{m}$ excess. $70\mu\text{m}$ emission for all other objects (except 32 Ori) was statistically zero, implying a non-detection. For 32 Ori, we detected emission consistent with predicted photospheric flux.

Interestingly, HD 35656 has one of the largest $24\mu\text{m}$ excesses among objects of similar ages. The ratio of observed $24\mu\text{m}$ flux to intrinsic photospheric emission, as determined from the $K-[24]$ locus, is ~ 4.76 . Subtracting the predicted photospheric flux from the observed flux indicates that emission from a putative disk is $\sim 376\%$ greater than that from the star alone. Balog et al. (2009) searched the literature and determined that only 8 other objects, including an object from their survey and excluding HD 21362 (due to free-free emission; Rieke et al. 2005), had $24\mu\text{m}$ excesses greater than 4 times their photospheric values at ages >20 Myr.

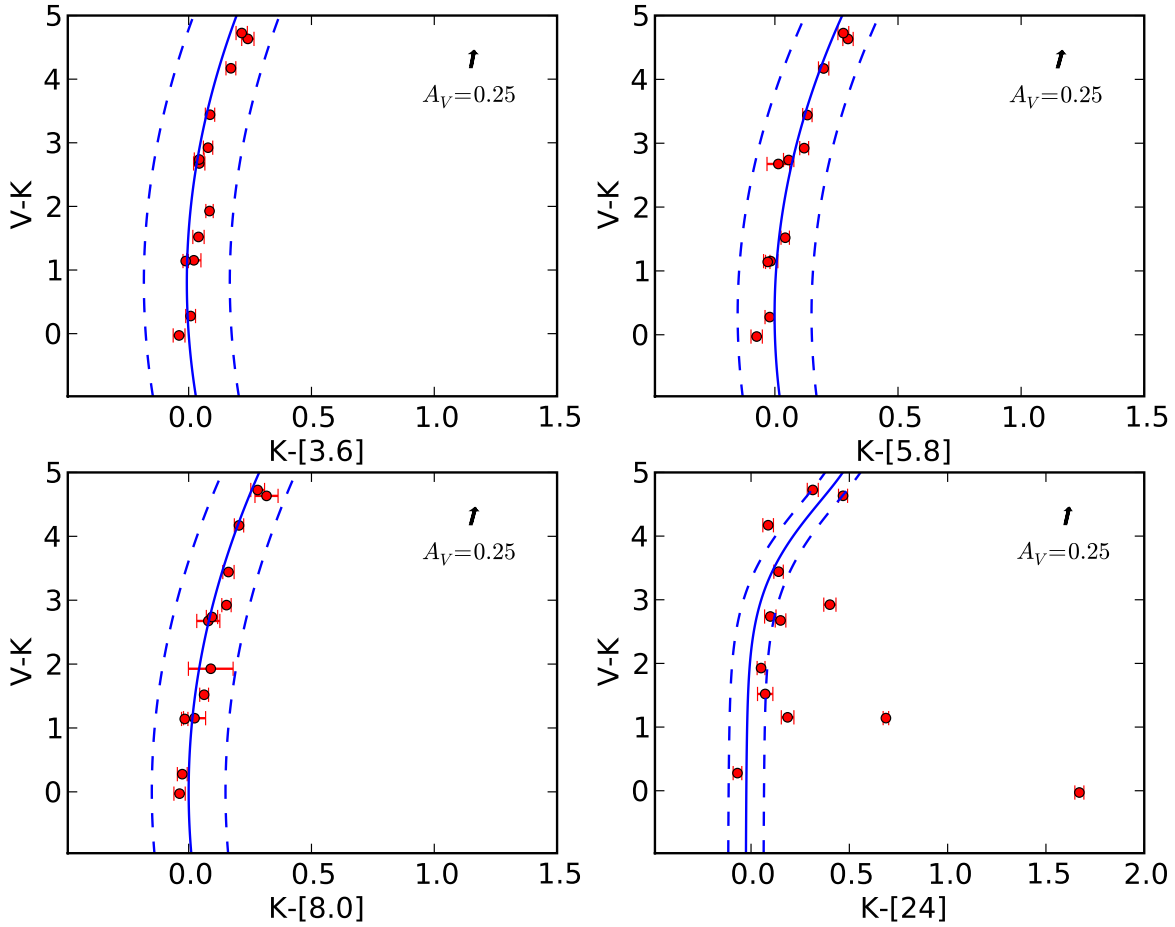


Figure 3. $V - K_s$ vs. $K_s - [\lambda_{\mu m}]$ color-color diagrams of 32 Ori group members. The solid line in each plot represent the zero-excess locus from Balog et al. (2009); the dashed lines represent the 3σ rms scatter ($\sim 17.5\%$, $\sim 15\%$, $\sim 15\%$, and $\sim 9\%$, respectively). Horizontal error bars represent 1σ photometric errors. In each plot, the vector A_V represents the average reddening towards group members.

Implications of the IR excess fraction and values will be discussed in §5.

6. STELLAR AND DISK MODELING

6.1. Stellar Photospheres

We modeled spectral energy distributions (SEDs) of our target stars by fitting ATLAS9 models of Castelli & Kurucz (2004) to $BVJHK_s$ & IRAC photometry. For M-type stars (i.e. 2UCAC 33699961 & 2UCAC 33878694), we used NextGen model atmospheres (Hauschildt et al. 1999) since ATLAS9 models do not extend to that temperature range (i.e. < 3500 K). We determined photospheric temperatures from spectral types and assumed solar metallicity, surface gravity $\log(g) = 4.5$, and a microturbulence of 2 km/s for all objects. We interpolated between temperature bins of existing models to obtain new models corresponding to the temperatures of our objects. We computed model fluxes by convolving atmospheric models with spectral response functions for each passband (i.e. Johnson B & V , 2MASS JHK_s , and IRAC ch1-ch4). The spectral response functions for the Johnson B & V passbands were obtained from Bessell (1990), 2MASS passbands were obtained from the Asiago Database on Photometric Systems (ADPS) (Fiorucci & Munari 2003), and the IRAC passbands for both full array and subarray mode

were obtained from the SSC website¹⁰. We interpolated models to the wavelength range for each passband, then determined model fluxes according to equation (3), where F_{λ_i} is the model flux at a given wavelength λ_i , $T(\lambda_i)$ is the spectral response function at that wavelength, and $\Delta\lambda_i$ is the wavelength step.

$$F_{\lambda} = \frac{\sum F_{\lambda_i} T(\lambda_i) \Delta\lambda_i}{\sum T(\lambda_i) \Delta\lambda_i} \quad (3)$$

ATLAS9 model atmospheres are sparsely sampled at wavelengths longer than $20 \mu m$; therefore, we interpolated between points, adopting a Rayleigh-Jeans functional dependence, as suggested in Carpenter et al. (2008) Appendix C2. Additionally, we “reddened” model fluxes according to the extinction curve defined by Fitzpatrick & Massa (2007), thereby allowing us to have A_V as a fitting parameter. We used the mean Galactic curve determined for the diffuse ISM and adopted $R(V) = 3.1$. Finally, we fit model fluxes to observed fluxes by implementing bounded chi-squared minimization, requiring that $A_V \geq 0$.

Stellar parameters are presented in Table 2. Final values for A_V were computed by averaging A_V derived from multiple colors (i.e. $B - V$, $V - I_c$, $V - J$, $V - H$, $V - K_s$, $J - H$, $H - K_s$,

¹⁰ <http://ssc.spitzer.caltech.edu/irac/calibrationfiles/spectral-response/>

Table 3
Stellar & Disk Parameters

ID	SpT.	A_V	T_* (K)	$\log \frac{L_*}{L_\odot}$	$\frac{M_*}{M_\odot}$	$\frac{L_{IR}}{L_{bol}}$	T_{disk} (K)	D (AU)	Zodies	$L_{IR} > f_{max}$
32 Ori	B5V	0.06	15206	2.68	4.5
HD 35656 ^a	A0Vn	0.00	9707	1.37	2.2	1.5×10^{-4}	94	42	2.6×10^6	n
HD 35714	A3	0.00	8503	1.06	1.8	$< 2.3 \times 10^{-5}$	< 22	< 540	$< 6.3 \times 10^7$	n
HD 35499 ^b	F4	0.13	6609	0.43	1.3	$< 3.7 \times 10^{-5}$	< 215	< 19	$< 1.2 \times 10^5$	n
						$> 3.0 \times 10^{-5}$	> 83	> 3	$> 2.1 \times 10^3$	n
HD 36338 ^b	F4.5	0.00	6560	0.46	1.3	$< 1.4 \times 10^{-4}$	< 215	< 14	$< 2.2 \times 10^5$	n
						$> 1.2 \times 10^{-4}$	> 97	> 3	$> 1.0 \times 10^4$	y
HD 35695	F9	0.20	6042	0.25	1.2	$< 1.5 \times 10^{-4}$	< 52	< 38	$< 2.0 \times 10^6$	n
HD 245567	G5	0.49	5738	0.23	1.2	$< 1.5 \times 10^{-4}$	< 50	< 41	$< 2.3 \times 10^6$	n
HBC 443	G7	0.98	5560	0.28	1.3	$< 1.5 \times 10^{-4}$	< 58	< 32	$< 1.5 \times 10^6$	n
RX J0520.5+0616 ^b	K3	0.60	4782	-0.35	0.9	$< 2.8 \times 10^{-4}$	< 215	< 10	$< 2.8 \times 10^5$	n
						$> 1.4 \times 10^{-4}$	> 71	> 1	$> 1.6 \times 10^3$	y
RX J0520.0+0612 ^a	K4	0.26	4600	-0.42	0.9	3.0×10^{-4}	51	18	9.5×10^5	n
RX J0523.7+0652	K6.5	0.17	4164	-0.70	0.7	$< 6.5 \times 10^{-4}$	< 43	< 18	$< 2.0 \times 10^6$	n
RX J0529.3+1210	K6.5	0.76	4164	-0.72	0.7	$< 7.5 \times 10^{-3}$	< 22	< 63	$< 2.9 \times 10^8$	n
2UCAC 33699961	M3	0.09	3274	-1.30	0.2	$< 1.4 \times 10^{-3}$	< 51	< 7	$< 6.0 \times 10^5$	n
2UCAC 33878694	M3	0.07	3274	-1.17	0.2	$< 6.3 \times 10^{-3}$	< 22	< 41	$< 1.0 \times 10^8$	n

Note. — ^a Disk models constrained by two mid-IR data points, therefore values are not upper limits. ^b Disk models include both Wien temperature fit and modified blackbody fit.

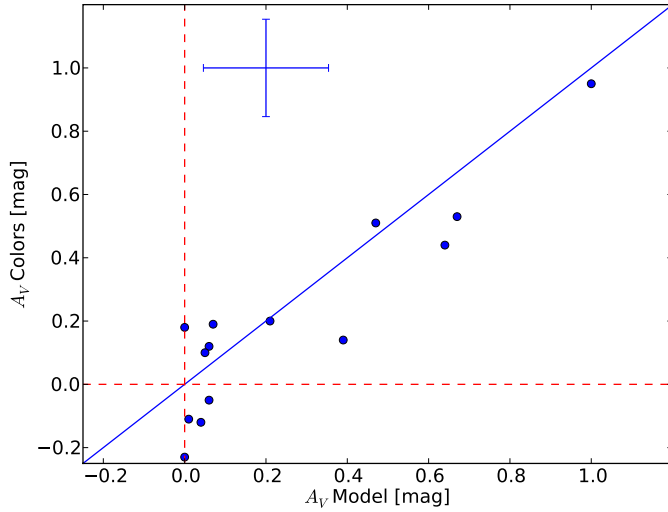


Figure 4. $A_{V,fit}$ vs. $A_{V,colors}$ for group members shows a near one-to-one correspondence. Error bars correspond to an rms deviation of 0.15 mag.

$J-K_s$, where available) with A_V determined from the fitting procedure, rounding negative values of A_V to 0. A plot of $A_{V,fit}$ vs. $A_{V,colors}$ (Fig. 3) shows an approximate one-to-one correspondence. The rms of the scatter, 0.15 mag, was comparable to the uncertainty in A_V corresponding to a shift of one spectral type. Similarly, the rms was comparable to the standard deviation of A_V derived from multiple colors. Thus, we conclude that A_V derived using both methods yield similar values¹¹.

Stellar temperatures presented in Table 2 were derived from spectral type and values for $\log(L_*/L_\odot)$ were obtained by integrating unreddened model atmospheres. Uncertainties in T_* and $\log(L_*/L_\odot)$ correspond to a \pm shift of one spectral type. Using these temperatures, luminosities, and their corresponding uncertainties, we constructed a theoretical

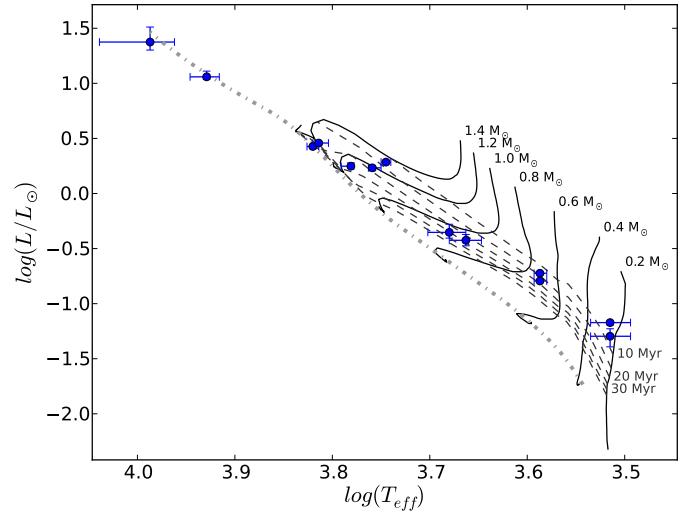


Figure 5. Theoretical H-R diagram for the observed 32 Ori members. Evolutionary tracks and isochrones are from Baraffe et al. (1998), which do not extend to masses greater than $1.4 M_\odot$. We have also plotted a 250 Myr isochrone from Dotter et al. (2008) to represent the main sequence for higher mass members. Error bars correspond to ΔL_* and ΔT_* resulting from a \pm shift in spectral type.

H-R diagram (Fig. 4). We interpolated the pre-main sequence evolutionary tracks of Baraffe et al. (1998) in order to fit the data and determined mean age for the association of 21 ± 15 Myr (1σ). Stellar photospheres are plotted with photometry in Figure 5.

6.2. Dust Disks

We sought to characterize mid-IR excesses of 32 Ori members by fitting models of dust emission to the 24 and 70 μ m photometry. We modeled disk emission as either blackbody radiation or modified blackbody radiation (i.e. $S_\nu \propto \nu^\beta B(\nu)$), depending upon the particular circumstance, in order to obtain upper and lower limits on disk parameters, like disk temperature, luminosity, radius, and emitting area. Lack of additional photometry makes higher order disk modeling

¹¹ Updated estimates of the interstellar reddening in Bell, Murphy, and Mamajek (submitted to MNRAS) are now consistent with small values ($E(B-V) \simeq 0.03 \pm 0.02$ mag) for both the hot and cool stars.

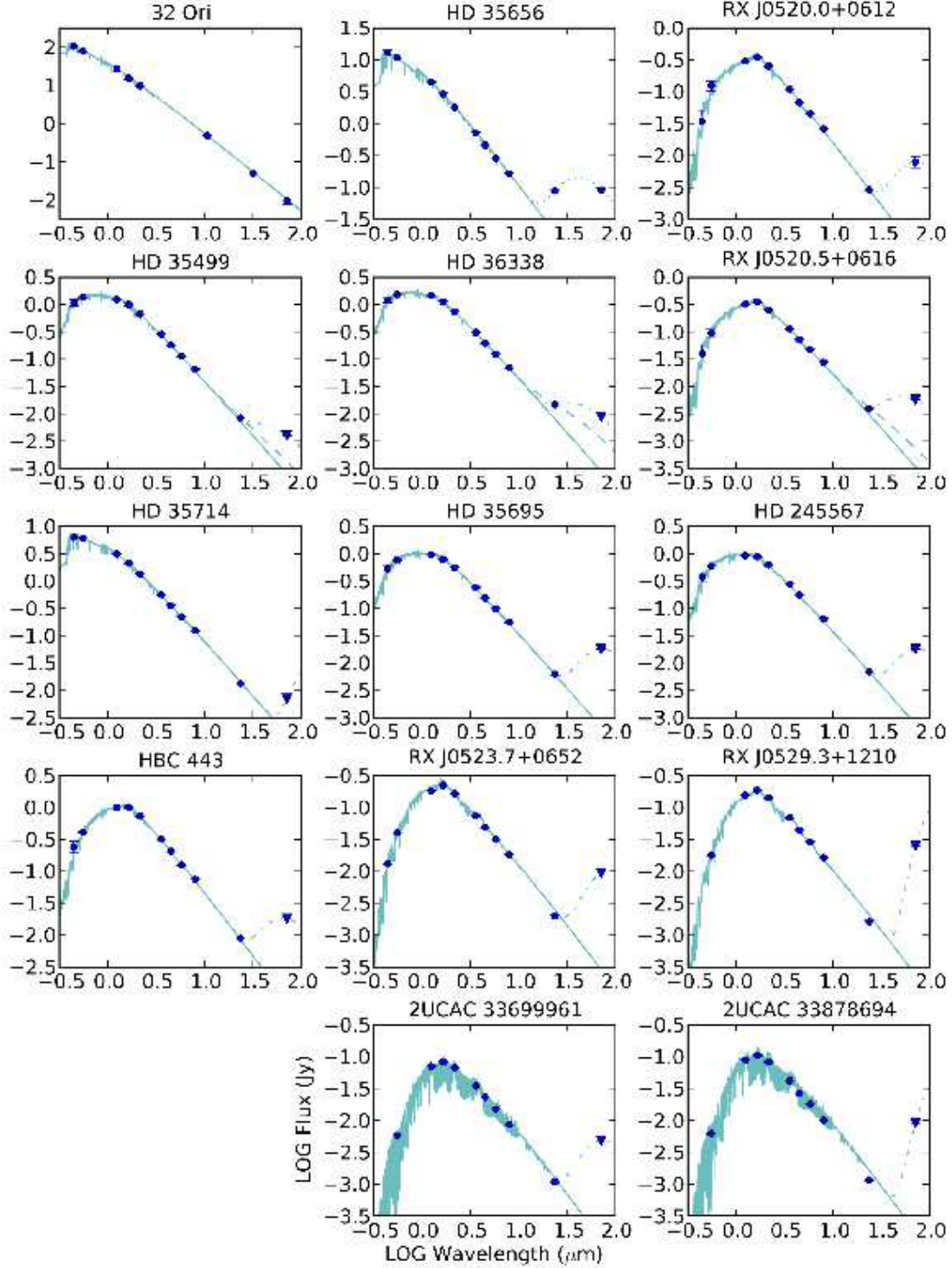


Figure 6. ATLAS9 model atmospheres were fit to $BVJHK_s$ & IRAC data, when available (only $BVJHK_s$ data for 32 Ori). NextGen model atmospheres were used for M-type stars (i.e. 2UCAC 33699961 & 2UCAC 33878694). For HD 35656 and RX J0520.0+0612, modified blackbody curves were fit to both 24 & 70 μm detections (dotted line). For the other 3 objects that exhibited 24 μm excesses, upper and lower limits for disk parameters were obtained by fitting two curves: a blackbody curve corresponding to a 24 μm Wien temperature (dashed line), and modified blackbody curve fit to 24 μm observations and 70 μm 3 σ upper limits (dash-dotted line). For all other objects, modified blackbody curves were used to model circumstellar disks by fitting 24 μm observations and 70 μm 3 σ upper limits (dash-dotted curve). These fits provide upper limits for disk parameters.

unwarranted as such models would be poorly constrained.

Modeling disk emission as blackbody radiation gives an upper limit for the true dust temperature (Carpenter et al. 2009), whereas a modified blackbody, which more closely resembles grain emission, yields a lower limit for the dust temperature. This is apparent from the Wien displacement law, which yields a higher temperature for a simple blackbody than for a modified blackbody (i.e. equation 4, which is accurate to within 0.5% for $\beta \in [0, 2]$).

$$T_{BB}(\nu_0) \approx (0.384\beta + 1) T_{mod BB}(\nu_0) \quad (4)$$

Disk radius is inversely proportional to disk temperature in that models that yield warmer disk temperatures predict smaller disk radii; therefore, blackbody models give a lower limit on disk radius and modified blackbody models give an upper limit. The same is true of the emitting area of the disk. For the modified blackbody model that we consider, we adopt $\beta = 0.8$, following Carpenter et al. (2009). This value is derived from Williams & Andrews (2006), who constrained $\beta \in [0.6, 1.0]$ with sensitive submillimeter observations of a small sample of debris disks.

There were four permutations of 24 and 70 μm excesses that were observed: HD 35656 had both 24 and 70 μm excesses; RX J0520.0+0612 had no 24 μm excess but a 70 μm excess; HD 36338, RX J0520.5+0616, and HD 35499 had 24 μm excesses and no 70 μm detections; and the other eight objects had no 24 μm excesses and no 70 μm detections. 32 Ori exhibited no mid-IR excess; observations at 10.75, 32, and 70 μm are all consistent with photospheric emission. We now consider these cases separately.

First, we subtracted predicted photospheric emission from observed fluxes and fit to these data. For HD 35656 and RX J0520.0+0612, we modeled the emission from the disk by fitting a modified blackbody curve to the 24 and 70 μm excess fluxes. For HD 36338, RX J0520.5+0616, and HD 35499, we obtained one range of limits by fitting a blackbody curve to the 24 μm excess flux only, adopting a 24 μm Wien temperature. Then we fit both the 24 μm excess flux and the 70 μm 3 σ upper limit with a modified blackbody curve.

Finally, for the 8 other objects that exhibited no 24 μm photospheric excess and whose 70 μm flux was statistically zero, we again fit modified blackbody curves to 24 μm data and 70 μm 3 σ upper limits, subtracting the photospheric component. Thus, these SEDs enabled us to compute upper limits for disk parameters. Values obtained from these fits are reported in Table 2.¹²

Ultimately, we determined dust temperatures within the range of $T_{gr} = 22\text{--}215\text{K}$ and fractional infrared luminosities within the range $L_{IR}/L_* = 2.3 \times 10^{-5} \text{--} 6.3 \times 10^{-3}$, the latter by integrating under the model. As mentioned above, we calculated two other important properties of the disk candidates that we observed: the emitting area and grain distance. Assuming that the zodiacal emission from our own solar

system is a single temperature blackbody, with $T = 260\text{K}$ (Reach et al. 1996) and $L_{IR}/L_* = 8 \times 10^{-8}$ (Good et al. 1986, see also Gaidos (1999) and Mamajek et al. (2004)), the emitting area of dust around another star in zodys (Z) is

$$A_{dust} = \left(\frac{T_{disk}}{260\text{K}} \right)^{-4} \left(\frac{L_{IR}/L_*}{8 \times 10^{-8}} \right) Z \quad (5)$$

Also, the ‘‘characteristic grain distance’’ D (Chen et al. 2005), which is derived from the radiative equilibrium equation of Jura et al. (1998), is

$$D = \frac{1}{2} \left(\frac{T_*}{T_{disk}} \right)^2 R_* \quad (6)$$

In this equation, T_* is the stellar photospheric temperature derived from spectral type, T_{disk} is the dust grain temperature, and R_* is the stellar radius derived from the Stefan-Boltzmann equation (i.e. $L_* = 4\pi R_*^2 \sigma T_*^4$). These properties are also listed in Table 2.

7. DISCUSSION

We place this group in context with previous studies of young stellar associations by comparing its debris disk fraction with those of groups compiled by Carpenter et al. (2009). Several caveats must be taken into consideration when making such comparisons. Firstly, debris disk fraction has been shown to depend on spectral type (e.g. Carpenter et al. 2009). Thus, in order not to be biased, it is important that the debris disk surveys that we compare have comparable sensitivity to lower mass stars; in other words, they cover the same range in mass (i.e. spectral type). We chose to include groups encompassing a spectral type range from B-M, which is the

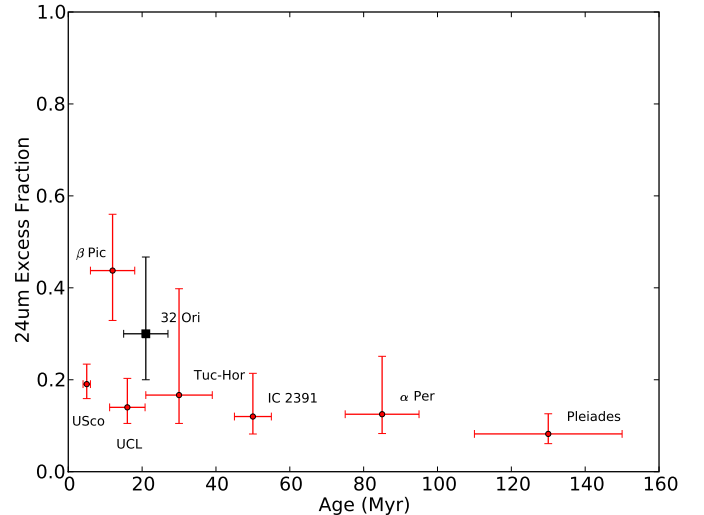


Figure 7. Debris disk fraction vs. age for the following groups: Upper Sco, β Pic, UCL, Tucana-Horologium, IC 2391, α Per, Pleiades (circles), and 32 Ori (square). Error bars correspond to 1 σ uncertainties in age and debris disk fraction, using binomial statistics. Disk fraction, ages, and spectral type range were obtained from Carpenter et al. (2009) and references therein. *Note to reader: Updated ages from Pecaut & Mamajek (2016) (10 ± 3 Myr for US, 16 ± 2 Myr for UCL) and Bell et al. (2015) (24 ± 3 Myr for β Pic Moving Group and 45 ± 4 Myr for Tuc-Hor) supercede the values used in this figure from 2010.*

¹² Parameters computed from 70 μm 3 σ upper limits should be interpreted in the following way: there is a 99.7% probability that the true parameter is less than the parameter that is presented.

(2009), various surveys adopt different excess thresholds and it is therefore necessary to define a common threshold. Ultimately, for the seven groups that we compare to 32 Ori (e.g. Upper Sco, β Pic, UCL, Tucana-Horologium, IC 2391, α Per, and Pleiades), we used a consistent $24\ \mu\text{m}$ excess threshold of $\geq 32\%$. A plot of debris disk fraction vs. age for the groups that meet these standards is presented in Figure 6.

We find that the debris disk fraction of the 32 Ori group is consistent with disk fractions for groups of comparable ages and that 32 Ori is, in fact, the 2nd “dustiest” group after the β Pic moving group, among those lacking accreting stars. The average excess fraction of the seven groups is 18% and the sample standard deviation is 12%. Thus, the $24\ \mu\text{m}$ disk fraction of the 32 Ori group is within 1σ of this mean.

We now consider further the large excess exhibited by HD 35656 ($\frac{L_{\text{IR}}}{L_*} = 1.5 \times 10^{-4}$). Is such an excess representative of steady-state collisional evolution, or must it have been caused by other means, such as a collisional event or feeding from an outer disk? Wyatt et al. (2007) considered the collisional evolution of debris disks around sun-like stars and derived a function that defines the maximum dust luminosity of a disk as a function of stellar mass, luminosity, age, and inner dust radius: $L_{\text{IR}}/L_{\odot} < 0.16 \times 10^{-3} M_*^{-5/6} L_*^{1/2} r_{\text{disk}}^{7/3} t^{-1}$. For a given object, excess emission above this maximum luminosity would require an additional, “transient” production mechanism. Wyatt et al. (2007) note that the most likely additional dust production mechanism is collisional grinding of planetesimals scattered inward from an outer belt (e.g. Beichman et al. 2005). Although HD 35656 has among the largest $24\ \mu\text{m}$ excesses compared to stars > 20 Myr, we found that its IR luminosity was consistent with steady state disk evolution, according to the equation of Wyatt et al. (2007).

Two stars, HD 36338 and RX J0520.5+0616, had IR luminosities that were greater than their respective maximum dust luminosities, suggesting that the IR excesses of these objects are unlikely to have resulted from steady state evolution. This result occurred only for models that assumed a $24\ \mu\text{m}$ Wien temperature of $T = 215\text{ K}$. Wien temperature models produced IR luminosities that were nominally equal to or less than models fit to both $24\ \mu\text{m}$ observations and $70\ \mu\text{m}$ 3σ upper limits. However, Wien temperature models produced characteristic grain distances that were much smaller than the latter model, resulting in a lower *maximum* dust luminosity. If, in fact, these objects are simply undergoing steady state evolution, their respective characteristic grain distances would have to be ≥ 5 AU and ≥ 3 AU, assuming that their IR luminosities remain the same. Detection of IR excesses at longer wavelengths would produce models with greater grain distances, likely resulting in fractional IR luminosities that satisfy steady state disk evolution.

8. SUMMARY

We have obtained IRAC 3.6, 4.5, 5.8 and $8\ \mu\text{m}$ photometry, MIPS 24 and $70\ \mu\text{m}$ photometry, and FAST low-resolution optical spectroscopy photometry of 14 members of the 32 Ori group. From the optical spectroscopy, we determined spectral types and effective temperatures for group members. We chose ATLAS9 or NextGen models corresponding to these temperatures and performed bounded chi-squared

fitting to optical and near-IR data. By integrating over complete atmospheric models, we determined more precise stellar luminosities for group members, which enabled us to construct an HR diagram and determine the age of the 32 Ori group using Baraffe et al. (1998) pre-main sequence tracks. Using similar methods, we fit models of disk emission to *Spitzer* 24 and $70\ \mu\text{m}$ fluxes in order to determine disk parameters. Ultimately, we conclude the following:

- No 32 Ori members exhibit near-IR excesses in IRAC bands ($3.6\text{--}8\ \mu\text{m}$), and thus we conclude that they lack warm inner dust disks. Spectroscopic results corroborate these findings and imply that none of the members are accreting.
- 4 objects exhibit $24\ \mu\text{m}$ excesses at least 4σ above their stellar photospheres, indicating that these members are debris disk candidates. This corresponds to a $24\ \mu\text{m}$ disk fraction of 29% (+14%, -9%). Only one of the $24\ \mu\text{m}$ excess objects, HD 35656, had an excess at $70\ \mu\text{m}$; however, we detected a $70\ \mu\text{m}$ excess for RX J0520.0+0612, which did not have a $24\ \mu\text{m}$ excess.
- For the two objects which had both 24 and $70\ \mu\text{m}$ detections (HD 35656 and RX J0520.0+0612), their fractional infrared luminosities, disk temperatures, disk inner edges, and emitting areas are as follows: $L_{\text{IR}}/L_* = 1.5 \times 10^{-4}$, 3.2×10^{-4} ; $T_{\text{gr}} = 94, 51\text{ K}$; $D = 43, 18\text{ AU}$; and $A_{\text{dust}} = 2.6 \times 10^6, 9.5 \times 10^5\text{ Z}$, respectively. Objects exhibiting $24\ \mu\text{m}$ excesses and no $70\ \mu\text{m}$ excess had disk parameters within the following ranges: $L_{\text{IR}}/L_* = 3.0 \times 10^{-5} - 2.8 \times 10^{-4}$; $T_{\text{gr}} = 71 - 215\text{ K}$; $D = 1 - 19\text{ AU}$; and $A_{\text{dust}} = 1.6 \times 10^3 - 2.8 \times 10^5\text{ Z}$.
- The 32 Ori group is similar to groups with comparable ages in its debris disk fraction and has the second highest $24\ \mu\text{m}$ excess fraction among groups lacking accreting T Tauri stars (behind only the β Pic moving group). Examining the fractions of debris disks, as determined by exhibiting a $24\ \mu\text{m}$ excess $\geq 32\%$ of the stellar photosphere, within groups encompassing a mass range from B-M spectral type, we find that the disk fraction within the 32 Ori group is statistically consistent with the average disk fraction of the 7 groups that fit this criteria.
- HD 35656 has a $24\ \mu\text{m}$ excess that is among the highest for objects > 20 Myr; however, its IR luminosity is consistent with steady state disk evolution. Wien temperature models of HD 36338 and RX J0520.5+0616 produce IR luminosities that exceed their respective maximum dust luminosities. A transient event may be required to explain such high luminosities; however, a larger characteristic grain distance than predicted by the Wien model would be consistent with steady state disk evolution.

The characteristics of the debris disks in the 32 Ori group in addition to the overall frequency of disks within the group

seem typical compared to groups of similar ages. If more low mass 32 Ori group members exist, perhaps their statistics will yield a lower overall debris disk fraction. The proximity of the group makes 32 Ori a unique laboratory to further examine debris disk properties.

This work is based on observations made with the *Spitzer Space Telescope*, which is operated by JPL/Caltech under a contract with NASA. The project was supported by NASA contract 1361947, administered through JPL. Part of this research was carried out at the Jet Propulsion Laboratory, California Institute of Technology, under a contract with the National Aeronautics and Space Administration. EEM and MJP also acknowledge support from the School of Arts and Sciences from the University of Rochester. This publication makes use of data products from the Two Micron All Sky Survey, which is a joint project of the University of Massachusetts and the Infrared Processing and Analysis Center/California Institute of Technology, funded by the National Aeronautics and Space Administration and the National Science Foundation. This paper has been approved for unlimited release (record URS263148, CL #16-6146). Facilities: Spitzer, CTIO:1.5m, CTIO:2MASS, FLWO:2MASS, FLWO:1.5m, HIPPARCOS.

REFERENCES

- Alcalá, J. M., Covino, E., Torres, G., Sterzik, M. F., Pfeiffer, M. J., & Neuhäuser, R. 2000, *A&A*, 353, 186
- Alcalá, J. M., et al. 1996, *A&AS*, 119, 7
- Backman, D. E., & Paresce, F. 1993, in *Protostars and Planets III*, ed. E. H. Levy & J. I. Lunine, 1253–1304
- Balog, Z., Kiss, L. L., Vinkó, J., Rieke, G. H., Muzerolle, J., Gáspár, A., Young, E. T., & Gorlova, N. 2009, *ApJ*, 698, 1989
- Barrado y Navascués, D., & Martín, E. L. 2003, *AJ*, 126, 2997
- Baraffe, I., Chabrier, G., Allard, F., & Hauschildt, P. H. 1998, *A&A*, 337, 403
- Beichman, C. A., et al. 2005, *ApJ*, 626, 1061
- Bell, C. P. M., Mamajek, E. E., & Naylor, T. 2015, *MNRAS*, 454, 593
- Bessell, M. S. 1990, *PASP*, 102, 1181
- Burgasser, A. J., Kirkpatrick, J. D., Reid, I. N., Brown, M. E., Miskay, C. L., & Gizis, J. E. 2003, *ApJ*, 586, 512
- Canup, R. M. 2004, *ARA&A*, 42, 441
- Carpenter, J. M., et al. 2008, *ApJS*, 179, 423
- . 2009, *ApJS*, 181, 197
- Castelli, F., & Kurucz, R. L. 2004, *ArXiv Astrophysics e-prints*
- Chen, C. H., Jura, M., Gordon, K. D., & Blaylock, M. 2005, *ApJ*, 623, 493
- Chen, C. H., et al. 2006, *ApJS*, 166, 351
- Dotter, A., Chaboyer, B., Jevremović, D., Kostov, V., Baron, E., & Ferguson, J. W. 2008, *ApJS*, 178, 89
- Ducourant, C., Teixeira, R., Périé, J. P., et al. 2005, *A&A*, 438, 769
- Engelbracht, C. W., et al. 2007, *PASP*, 119, 994
- Fiorucci, M., & Munari, U. 2003, *A&A*, 401, 781
- Fitzpatrick, E. L., & Massa, D. 2007, *ApJ*, 663, 320
- Gaidos, E. J. 1999, *ApJL*, 510, L131
- Good, J. C., Gautier, T. N., & Hauser, M. G. 1986, *Advances in Space Research*, 6, 83
- Gray, R. O., & Corbally, C., J. 2009, *Stellar Spectral Classification by Richard O. Gray and Christopher J. Corbally*. Princeton University Press
- Haisch, Jr., K. E., Lada, E. A., & Lada, C. J. 2001, *ApJL*, 553, L153
- Hauschildt, P. H., Allard, F., Ferguson, J., Baron, E., & Alexander, D. R. 1999, *ApJ*, 525, 871
- Hernández, J., Briceño, C., Calvet, N., Hartmann, L., Muzerolle, J., & Quintero, A. 2006, *ApJ*, 652, 472
- Hillenbrand, L. A. 2005, *ArXiv Astrophysics e-prints*
- . 2008, *Physica Scripta Volume T*, 130, 014024
- Høg, E., et al. 2000, *A&A*, 355, L27
- Jura, M., Malkan, M., White, R., Telesco, C., Pina, R., & Fisher, R. S. 1998, *ApJ*, 505, 897
- Mace, G. N., Prato, L., Wasserman, L. H., Schaefer, G. H., Franz, O. G., & Simon, M. 2009, *AJ*, 137, 3487
- Makovoz, D., & Marleau, F. R. 2005, *PASP*, 117, 1113
- Mamajek, E. E. 2007a, in *IAU Symposium*, Vol. 237, IAU Symposium, ed. B. G. Elmegreen & J. Palous, 442–442
- Mamajek, E. E. 2009, in *American Institute of Physics Conference Series*, Vol. 1158, *American Institute of Physics Conference Series*, ed. T. Usuda, M. Tamura, & M. Ishii, 3–10
- Mamajek, E. E., Meyer, M. R., Hinz, P. M., Hoffmann, W. F., Cohen, M., & Hora, J. L. 2004, *ApJ*, 612, 496
- Mamajek, E. E., Meyer, M. R., & Liebert, J. 2002, *AJ*, 124, 1670
- . 2006, *AJ*, 131, 2360
- Mentuch, E., Brandeker, A., van Kerkwijk, M. H., Jayawardhana, R., & Hauschildt, P. H. 2008, *ApJ*, 689, 1127
- Meyer, M. R., Backman, D. E., Weinberger, A. J., & Wyatt, M. C. 2007, *Protostars and Planets V*, 573
- Neuhäuser, R., Torres, G., Sterzik, M. F., & Randich, S. 1997, *A&A*, 325, 647
- Pecaut, M. J., & Mamajek, E. E. 2013, *ApJS*, 208, 9
- Pecaut, M. J., & Mamajek, E. E. 2016, *MNRAS*, 461, 794
- Pecaut, M. J., Mamajek, E. E., & Bubar, E. J. 2012, *ApJ*, 746, 154
- Perryman, M. A. C., & ESA, eds. 1997, *ESA Special Publication*, Vol. 1200, *The HIPPARCOS and TYCHO catalogues. Astrometric and photometric star catalogues derived from the ESA HIPPARCOS Space Astrometry Mission*
- Quijada, M. A., Marx, C. T., Arendt, R. G., & Moseley, S. H. 2004, in *Presented at the Society of Photo-Optical Instrumentation Engineers (SPIE) Conference*, Vol. 5487, *Society of Photo-Optical Instrumentation Engineers (SPIE) Conference Series*, ed. J. C. Mather, 244–252
- Reach, W. T., et al. 1996, *A&A*, 315, L381
- Reach, W. T., et al. 2005, *PASP*, 117, 978
- Rieke, G. H., et al. 2005, *ApJ*, 620, 1010
- Shvonski, A. J., Mamajek, E. E., Meyer, M. R., & Kim, J. S. 2010, *Bulletin of the American Astronomical Society*, 42, 428.22
- Torres, G., Neuhäuser, R., & Guenther, E. W. 2002, *AJ*, 123, 1701
- van Leeuwen, F. 2007, *Astrophysics and Space Science Library*, 350
- Williams, J. P., & Andrews, S. M. 2006, *ApJ*, 653, 1480
- Wyatt, M. C., Smith, R., Greaves, J. S., Beichman, C. A., Bryden, G., & Lisse, C. M. 2007, *ApJ*, 658, 569
- Young, E. T., et al. 2004, *ApJS*, 154, 428
- Zacharias, N., Urban, S. E., Zacharias, M. I., Wycoff, G. L., Hall, D. M., Monet, D. G., & Rafferty, T. J. 2004, *AJ*, 127, 3043 (UCAC2)
- Zacharias, N., Finch, C., Girard, T., et al. 2010, *AJ*, 139, 2184 (UCAC3)